

Sub-cycle multidimensional spectroscopy of strongly correlated materials

V. Valmispild

*Institute of Theoretical Physics, University of Hamburg, Notkestraße 9, 22607 Hamburg, Germany and
European XFEL, Holzkoppel 4, 22869 Schenefeld, Germany*

E. Gorelov

European XFEL, Holzkoppel 4, 22869 Schenefeld, Germany

M. Eckstein

Department of Physics, University of Erlangen-Nuremberg, 91058 Erlangen, Germany

A. Lichtenstein

*Institute of Theoretical Physics, University of Hamburg, Notkestraße 9, 22607 Hamburg, Germany
The Hamburg Centre for Ultrafast Imaging, Luruper Chaussee 149, 22761 Hamburg, Germany and
European XFEL, Holzkoppel 4, 22869 Schenefeld, Germany*

H. Aoki

*Department of Physics, The University of Tokyo, Hongo, Tokyo 113-0033, Japan and
National Institute of Advanced Industrial Science and Technology (AIST), Tsukuba 305-8568, Japan*

M. Katsnelson

*Institute for Molecules and Materials, Radboud University,
Heyendaalseweg 135, 6525AJ Nijmegen, The Netherlands*

M. Ivanov and O. Smirnova

Max-Born-Institut, Max-Born-Str. 2A, 12489 Berlin, Germany

(Dated: August 10, 2022)

Strongly correlated solids are extremely complex and fascinating quantum systems, where new states continue to emerge [1–3] and where interaction with light may trigger interplay between them [4]. In this interplay, sub-laser-cycle electron response is particularly attractive as a tool for ultrafast manipulation of matter at PHz scale [5–8]. Here we introduce a new type of non-linear multidimensional spectroscopy, which allows us to unravel the sub-cycle dynamics of strongly correlated systems interacting with few-cycle infrared pulses and the complex interplay between different correlated states evolving on the sub-femtosecond time-scale. For the two-dimensional Hubbard model under the influence of ultra-short, intense electric field transients, we demonstrate that our approach can resolve pathways of charge and energy flow between localized and delocalized many-body states on the sub-cycle timescale and follow the creation of a highly correlated state surviving after the end of the laser pulse. Our findings open a way to a regime of imaging and manipulating strongly correlated materials at optical rates, beyond the multi-cycle approach employed in Floquet engineering [9, 10] of quantum systems.

The advent of attosecond pulses [11–13], attosecond spectroscopy [14–23], and light-wave electronics [6, 24, 25], which aim to resolve and control light driven electron motion on sub-laser cycle time scales [5, 26–28], has challenged our perception of reactivity – a capacity of a substance, such as an atom, molecule or solid, to undergo changes triggered by an external agent. In chemistry, it prompted a quest for charge directed reactivity, that is, chemical change driven by attosecond electron dynamics [29–35]. Similar concept should exist in condensed matter systems, where strong electron-electron correlations can lead to a rich set of phase transitions and the appearance of new states of matter due to electronic response to intense light.

So far, investigation of light-driven changes in strongly correlated materials was focused on the Floquet regime [10], giving rise to the powerful concept of Floquet engineering of quantum materials [9], which typically focuses on laser-cycle-averaged modifications of material properties. Yet, in strongly correlated systems the sub-laser-cycle time scale is also highly relevant: a typical electron-electron interaction parameter $U \sim 1\text{eV}$ corresponds to the time-scale $\Delta t \sim 1/U \sim 1\text{ fs}$, well below the cycle of a standard infrared driver, with the respective dynamics potentially leading to such remarkable features such as e.g. a transition from Coulomb repulsion to effective electron-electron attraction induced by half-cycle pulses [36, 37].

Crucially, in correlated systems even modest light-induced modifications of the electron hopping rate between neighbouring sites may strongly affect the state of the system [10]. It opens fundamental questions related to measurement and control: How can we monitor strongly correlated electron response evolving on sub-laser-cycle time scale? Can we

control the outcome of light-induced changes in correlated materials, shaping electronic states of matter by tailoring the light field on sub-cycle scale to obtain properties on demand [38]?

One way to probe and control the sub-laser-cycle electronic response is to use few-cycle pulses with controlled carrier-envelope phase (CEP) [5, 27, 28, 39]. In solids, these pulses have been used to detect photoemission delays [40] and quantify the time-scale of non-linear response to light [41], image surface states in topological insulators [42], resolve and control highly non-linear electronic response in bulk dielectrics, 2D materials, and nano-structures [8, 18, 43–45]. Yet, the physical picture of electron-electron correlations evolving on the *sub-cycle* scale in strongly correlated systems remains elusive.

Here we introduce a sub-cycle multidimensional spectroscopy of electron dynamics in solids and apply it to a strongly correlated system. Our approach uses the CEP-dependence of the correlated multi-electron response to decode the complex interplay between different many-body states, triggered by the interaction with a few-cycle mid-IR control pulse. Ultimately, the analysis of the multi-dimensional spectra allows us to uncover the physical picture of the underlying correlated dynamics in this system, both in space and time.

The dynamics induced by strong low-frequency fields extends beyond the conventional Floquet-type analysis (see e.g. [9, 10]), which exploits cycle-averaged modifications of matter by periodic light fields, in several important aspects: When the peak voltage applied across a unit cell approaches the electron hopping rate, the correlated response can change significantly from one laser cycle to the next. This leads to non-adiabatic transitions between multiple Floquet states within a quarter of the laser cycle. The many-body state created by the field is shaped by these non-adiabatic dynamics during the pulse. As a result, after the laser pulse the system can remain in a different many-body final state, with energy and other variables sensitively depending on the highly nonlinear pump process. Therefore, the direct control of nonadiabatic excitation processes using strong multicolor laser fields structured in time and space [23, 24, 46] emerges as a promising pathway to reaching nontrivial metastable field-free correlated states. The possibility to spectroscopically analyze the underlying excitation pathways, as introduced below, is key to understanding non-thermal materials control.

We consider a half-filled Hubbard model on the two-dimensional square lattice for fermions, supporting a realistic two-dimensional band dispersion with the characteristic van Hove singularity and sharp band edges. The lattice is driven by intense, linearly-polarized field. In contrast to previously studied Bethe- or hypercube-lattices [37, 47] or one-dimensional chains [22], here the field can be applied either along one of the lattice directions, which will result in a quasi one-dimensional system [22, 48], or along the diagonal, which triggers a fully two-dimensional response.

To treat the non-perturbative time-dependent problem, we employ the non-equilibrium extension [49, 50] of the dynamical mean-field theory (DMFT) [51]. The algorithm and its realization are described in Ref. [52], see Methods for details. The method was benchmarked against exact diagonalization of one-dimensional finite chain used in [22], see Supplementary Information (SI). The implementation is based on the NESSi simulation package for non-equilibrium Green's functions [53].

For the present calculation, we adopt the hopping parameters for undoped La₂CuO₄ (LCO), with the lattice constant $a_0 = 3.78$ Angstrom. We use the single-band Hubbard model with the nearest-neighbour hopping parameter $T_1 = 0.43$ eV [54]. We set the Hubbard $U = 2.5$ eV, close to the estimate of Ref. 55. We use few-cycle pulses with central wavelength of $\lambda = 1500$ nm (with $\omega = 0.827$ eV) and duration of 7.7 fs (full width at half-maximum, FWHM), with a total simulation time 32.8 fs. The pulse polarization is parallel to the lattice diagonal ([11]) direction, so that both lattice directions are equally affected by the laser field. To demonstrate that our results are typical for the low-frequency regime $\omega \ll U$, we also present simulations for $\lambda = 3000$ nm ($\omega = 0.413$ eV).

Our results are summarized in Fig.1. Figures 1(a,c,e) show the temporal profile of the occupied density of states (see Methods) for the field strength increased from $F_0 = 0.1$ V/Å to 2.0V/Å. The voltage across a unit cell approaches the hopping rate, $a_0 F_0 \sim T_1$, at $F_0 \sim 0.1$ V/Å ($I_0 \sim 1.6 \times 10^{11}$ W/cm²). Thus $F_0 \sim 0.1$ V/Å could modify the effective hopping rate within the laser cycle and thus alter the structure of the correlated system.

Indeed, transfer of spectral weight from the quasi-particle peak (QP), located near zero energy, to the Hubbard bands becomes prominent as soon as the field approaches 0.1 V/Å. At this field (see Fig. 1(a)), after the transition at ~ 17.5 fs the spectral density remains predominantly in the lower Hubbard band and does not return back to the QP after the pulse is gone. Already for this lowest field strength, Fig. 1(a) hints at the importance of the sub-cycle response: the cycle-averaged renormalization of hopping $T_1 \rightarrow T_1 J_0(F_0 a_0 / \omega) = 0.97 T_1$ does not lead to any substantial changes in the spectral density, let alone to the major restructuring observed in Fig. 1(a) (see Supplementary Information).

At higher fields (Fig. 1(c,e)), we see substantial transfer of the spectral density to the upper Hubbard band (situated at $E = 1.25$ eV), with the electron density peaked at the energies corresponding to the upper and lower Hubbard bands. Crucially, this dichotomic structure survives well after the end of the pulse. Figures 1(a,c,e) thus signify transition from a metallic to a highly correlated state in which the light-driven current is fully quenched (see Fig.4(d) below.)

To understand these complex many-body dynamics, we first look at the cuts (Figure 1(b,d,f)) of the electron density for specific energies corresponding to the lower Hubbard band (LHB, $E = -1.25$ eV), upper Hubbard band

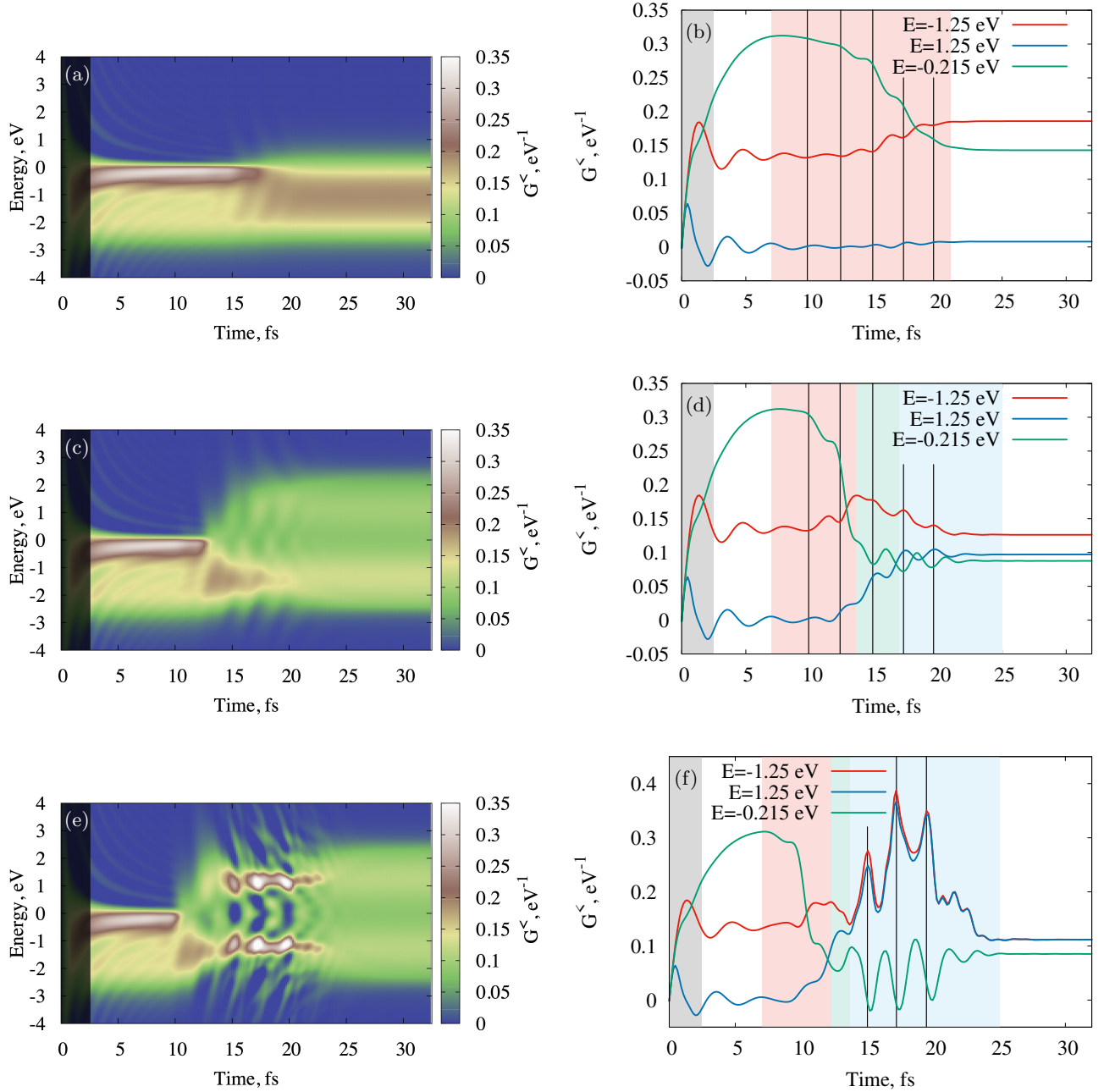


FIG. 1. Temporal evolution of density of states showing light-induced transition from metallic to Mott-insulating states. (a) $F_0=0.1$ V/A, (c) 0.5 V/A, (e) 2.0 V/A. Artifact of the Fourier transform which appears at 0-2.5 fs is covered by shadow. (b,d,f) Oscillations of electron density at energies corresponding to *LHB* ($E = -1.25$ eV, red), *UHB* ($E = 1.25$ eV, blue), and *QP* ($E = -0.215$ eV, green) for $F_0 = 0.1$ V/A (b), $F_0 = 0.5$ V/A (d) and $F_0 = 2$ V/A (f). Red, green and blue shading marks three different regimes of field-driven dynamics. Red shading: density at *LHB* and *UHB* oscillates out of phase; blue shading: locking regime, density at *LHB* and *UHB* oscillates in phase; green shading: intermediate regime.

(*UHB*, $E = 1.25$ eV) and *QP* (maximizing at -0.215 eV). The exchange of population in Fig. 1(d) has three distinct regimes, marked as three shaded areas: around 4-11 fsec (red), 11-16 fsec (green), and beyond 16 fsec (blue). The first regime (red shading) corresponds to the decreasing electron density at the energy corresponding to the *QP* peak and increasing density at the energies corresponding to *LHB* and *UHB* (see also Figure 1(b)), with the populations at *LHB* and *UHB* energies oscillating out of phase (see also Figure 1(b)). In the second regime (green shaded area in Figure 1(d)), the density at *UHB* energy raises, while the density at *LHB* energy decreases. The third regime is most surprising: we observe in-phase oscillations of electron density at *UHB* and *LHB* energies (blue shaded area

in Figure 1(d)). At higher intensities the electron densities at *UHB* and *LHB* energies become fully locked: both populations are equal and oscillate exactly in phase (blue shaded area at $t > 14$ fs in Figure 1(f)). The maxima of these locked populations are synchronized with the minima in the density located at the *QP*.

The locking of populations at three key energies of the system is a remarkable effect, which appears to be correlated with the onset of metal to insulator transition observed in Figs. 1(c,e). Cartoon in Fig. 2(a) illustrates the three key field-free many-body states of our system using the language of DMFT [56]. Characteristic many-body states contributing to the signal at *LHB* mainly involve electrons localized on singly occupied lattice sites, *QP* represents superposition of delocalized and localized electrons, while doubly occupied and unoccupied sites are the characteristic features of many-body states contributing to *UHB*. Analysis (see SI) of Fig. 1 (f) suggests that the rate of flow of electron density *from* *LHB* and *UHB* bands maximizes near zeroes of field oscillation ($F(t) \simeq 0$), while the rate of flow of electron density *to* *LHB* and *UHB* bands maximizes near instantaneous maxima of the field ($|F(t)| \simeq F_0$). This flow is indicated by the double headed arrows in Fig. 1 (f). The oscillations of the density at *QP* are in phase with the laser field: the minima coincide with $F(t) \simeq 0$, the maxima coincide with $|F(t)| \simeq F_0$.

However, Fig. 1 (f) does not reveal yet the sequence of states and transitions followed by the non-equilibrium charge distribution. For example, the flow of charge can proceed from *LHB* to *UHB* via *QP*, or it can follow two separate circuits: from *LHB* to *QP* and back to *LHB*, or *UHB* to *QP* and back to *UHB*. Fig. 1 (f) also does not specify the time-scale of various non-adiabatic transitions between laser-dressed states of the system, and it also does not tell us how many such states are populated during the pulse and thus contribute to the light-driven phase transition.

To decode the physics underlying the laser driven phase transition in our system and establish the role of sub-cycle electron dynamics we need a spectroscopy sensitive to such dynamics, which we introduce below. To this end, we exploit the full spectroscopic nature of the Keldysh Green's function $G^<(t, t - \tau)$, which can be retrieved from multi-pulse time and angular-resolved photoemission (trARPES) experiments (see e.g [57] and Supplementary material.)

Figures 1(b-d) show the Fourier image of such signal with respect to τ , yielding the population of the occupied states (with energy Ω_τ) prior to photo-ionization. The intense low-frequency field plays the role of a control pulse, which modifies our system between these two events. Thus, formally, we have a sequence of three pulses (Fig.2(b)) reminiscent, but not identical, to the set-up of non-linear 2D spectroscopy [58]. Fourier transforming $G^<(t, t - \tau)$ with respect to τ , selecting a value of Ω_τ , and Fourier transforming $G^<(t, \Omega_\tau)$ with respect to the delay t between the control pulse and the pump-probe pair, we obtain the spectrum of the states (transition frequencies) that the Floquet state associated with Ω_τ couples to (see Methods). Indeed, for the dynamics described by a single Floquet state, $G^<(t, \Omega_\tau)$ should behave periodically as a function of t , and its Fourier transform will only show the sidebands at $\pm n\omega$ (n is integer, see the ladder of red-brown peaks in Fig.2(c)). In contrast, in the presence of non-adiabatic transitions between the Floquet states, $G^<(t, \Omega_\tau)$ becomes aperiodic and its Fourier transform will show the new frequencies appearing due to non-adiabatic excitations (see green peaks in Fig.2(c).)

Last but not least, we can reveal the underlying sub-cycle dynamics by scanning the CEP ϕ_{CEP} of the IR (control) pulse and recording the resulting response $G^<(t, t - \tau, t_{CEP})$ as a function of $t_{CEP} = \phi_{CEP}/\omega$. The Fourier transform of $G^<(t, t - \tau, t_{CEP})$ with respect to t_{CEP} shows the speed of response: from instantaneous to cycle averaged. Individual Floquet states lack CEP dependence, apart from the trivial dependence on $t - t_{CEP}$, which we explicitly remove upon the Fourier transform (see Methods). Therefore, the broader the resulting spectrum with respect to the CEP (see schematic in Fig.2(c)), the stronger is the non-trivial CEP dependence, the stronger, faster, and more sensitive to the instantaneous electric field are the non-adiabatic transitions between the Floquet states.

As a result of the three Fourier transforms, we obtain a three dimensional set of data $G^<(\Omega_\tau, \Omega_t, \Omega_{CEP})$ exposing the correlations between all populated states of the system, tagged by Ω_{CEP} . The cutoff frequency Ω_{CEP}^{\max} in the spectrum indicates the fastest response time $\sim 1/\Omega_{CEP}^{\max}$ of the respective laser driven transitions between all states.

To visualize the frequency correlations encoded in $G^<(\Omega_\tau, \Omega_t, \Omega_{CEP})$ we fix Ω_τ and plot the resulting 2D spectrum $|G^<(\Omega_\tau, \Omega_t, \Omega_{CEP})|$ as a function of Ω_t (vertical axis) and Ω_{CEP} (horizontal axis), as schematically shown in Fig.2(c). The trivial CEP-dependence, characteristic of the standard Floquet regime, $G^<(\Omega_\tau, t, t_{CEP}) = G^<(\Omega_\tau, t - t_{CEP})$ is removed (see Methods). Fig 2(c) summarises the simple rules which help one to read these 2D spectra.

First, for each Ω_τ , the peaks appearing at $\Omega_t = 0$ correspond to energy specified by Ω_τ . Second, $\Omega_t > 0$ correspond to absorption from Ω_τ , $\Omega_t < 0$ correspond to emission from Ω_τ . Third, peaks at $\Omega_{CEP} = 0$ correspond to cycle-averaged (or one-photon) transitions. The spectral peaks along the CEP dimension are separated by even number of photons due to the left-right symmetry of infinite lattice. Their strength reflects the importance of sub-cycle dynamics and the ability of the system to respond to the instantaneous field.

Fig 3 shows the respective 2D spectra for all three intensities and for $\Omega_\tau = -1.25\text{eV}$ (*LHB*), $\Omega_\tau = 1.25\text{eV}$ (*UHB*). Applying the three rules formulated above, we see that at the lowest field strength ($F_0 = 0.1\text{V/\AA}$) and for $\Omega_\tau = -1.25\text{eV}$, the two peaks dominating the spectrum Fig.2(a) are at $\Omega_{CEP} = 0$. They correspond to *LHB* ($\Omega_t = 0$) and *QP* ($\Omega_t \simeq 1.25\text{eV}$). The coupling between *LHB* and *QP* is already quite strong: indeed, $F_0 a_0 \sim E_{QP} - (\omega + E_{LHB}) \sim \omega$ already at this field strength. Since the field-free system starts in *QP*, the $QP \leftrightarrow LHB$ coupling can be interpreted as localization due to field-induced suppression of tunnelling on the sub-cycle scale, as evidenced by the additional

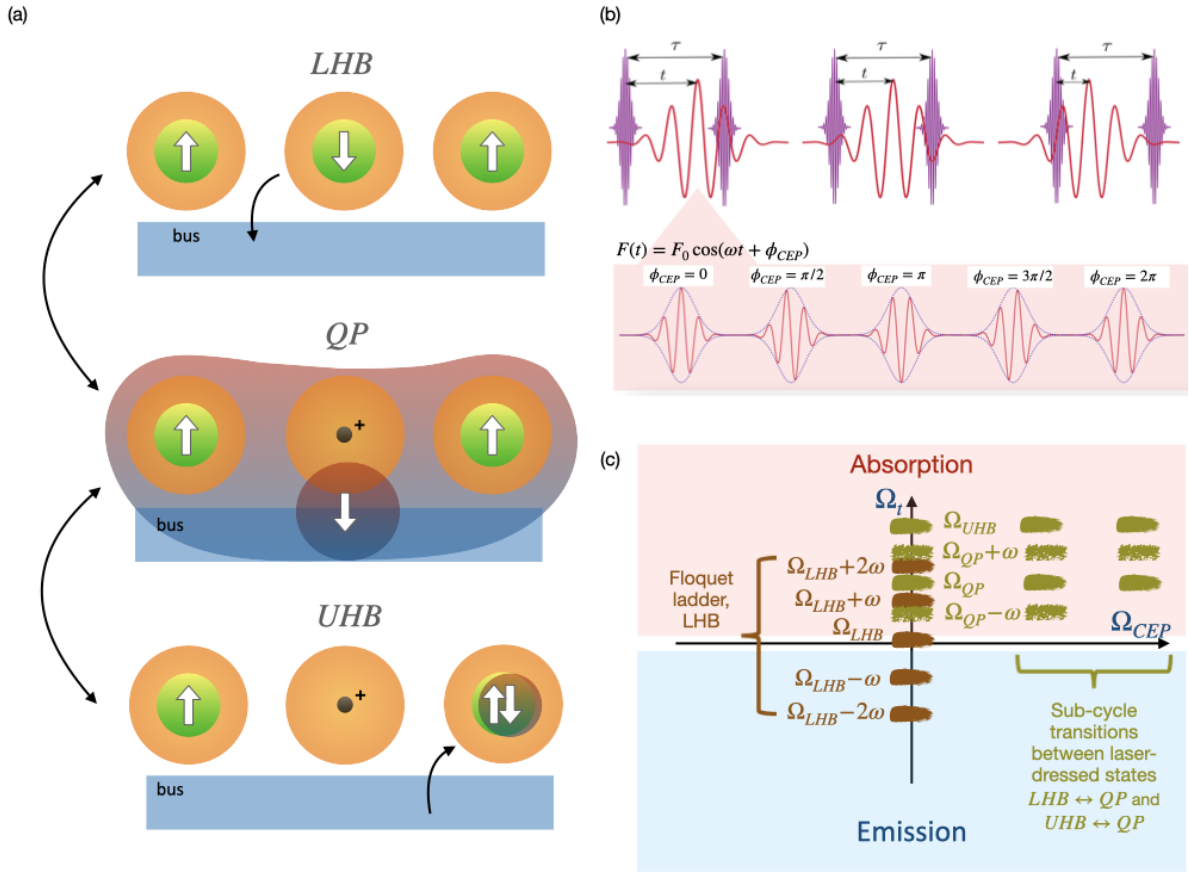


FIG. 2. Spectroscopic nature of the Keldysh Green function $G^<sup>\langle</math>. (a) Cartoon view of the key many-body states corresponding to the spectroscopic signal at the energies of LHB , QP , UHB . Double headed arrows indicate possible sub-cycle transitions driven by the field in the phase locking regime (see Fig. 1 (f)). (b) Scanning delay τ between the pump and probe pulses (violet), and delay t between the pump-probe pair and the control pulse (red), yields two dimensional data set for the Green function $G^<sup>\langle</math> ($t, t - \tau$) emulating photonization signal. Scanning the carrier-envelope phase (ϕ_{CEP}) of the control pulse yields the third dimension of the spectroscopic signal $G^<sup>\langle</math> ($t, t - \tau, \phi_{CEP}$). (c) Fourier transform of $G^<sup>\langle</math> ($t, t - \tau, \phi_{CEP}$) with respect to all arguments yields $G^<sup>\langle</math> ($\Omega_\tau, \Omega_t, \Omega_{CEP}$). Cartoon view of $|G^<sup>\langle</math> ($\Omega_\tau, \Omega_t, \Omega_{CEP}$)| for Ω_τ fixed at the energy corresponding to LHB . Red-brown peaks illustrate the Floquet ladder associated representing laser-dressed LHB state. The appearance of green peaks at $QP \pm n\omega$ and UHB is due to non-adiabatic transitions between the laser dressed states $LHB \leftrightarrow QP$ and $UHB \leftrightarrow QP$. The extension of green peaks in the Ω_{CEP} dimension quantifies the sub-cycle response time.$$$$$$

peaks at $\Omega_{CEP} = 2\omega$.

Fig.2(b) shows the 2D spectra for $\Omega_\tau = 1.25eV$ corresponding to UHB , for the same F_0 . The dominant peak at $\Omega_{CEP} = 0$ corresponds to the contribution of QP , signifying transitions between QP and UHB . The relative weakness of peaks at $\Omega_{CEP} \neq 0$ shows that their coupling is well described by cycle-averaged processes.

The situation is somewhat different for the intermediate field strength $F_0 = 0.5$ V/A, see Fig 3(c,d). Consider first $\Omega_\tau = -1.25eV$, corresponding to LHB (Fig. 3(c)). The peaks at $\Omega_{CEP} = 0$ correspond to the Floquet ladders associated with both QP and LHB, with broad overlapping steps. The CEP-sensitive dynamics becomes more significant in LHB-QP transitions. The dominant part of the upper peak at $\Omega_{CEP} = 2\omega$ is due to QP lifted by one photon or UHB .

The high-field regime ($F_0 = 2$ V/A) shown in Fig 3(e,f) corresponds to several new features in the spectrum. First, we see broad spectrum along the vertical axis for a wide range of CEP frequencies (horizontal axis). Second, the sub-cycle dynamics is very important and the spectrum has individual sub-cycle cut-offs: the highest positive and highest negative Ω_t depend on Ω_{CEP} . These cut-offs appear to be proportional to the instantaneous values of the laser field and increase with increasing $\Omega_{CEP} > 0$. Third, the overall 2D spectra are shifted towards positive values of Ω_t for LHB, corresponding to absorption, and negative values of Ω_t for UHB, corresponding to emission. The respective peaks at $\Omega_{CEP} = 4\omega$ (Fig 3(e)) and $\Omega_{CEP} = -4\omega$ (Fig 3(f)) indicate their strongly sub-cycle nature. Forth, while the

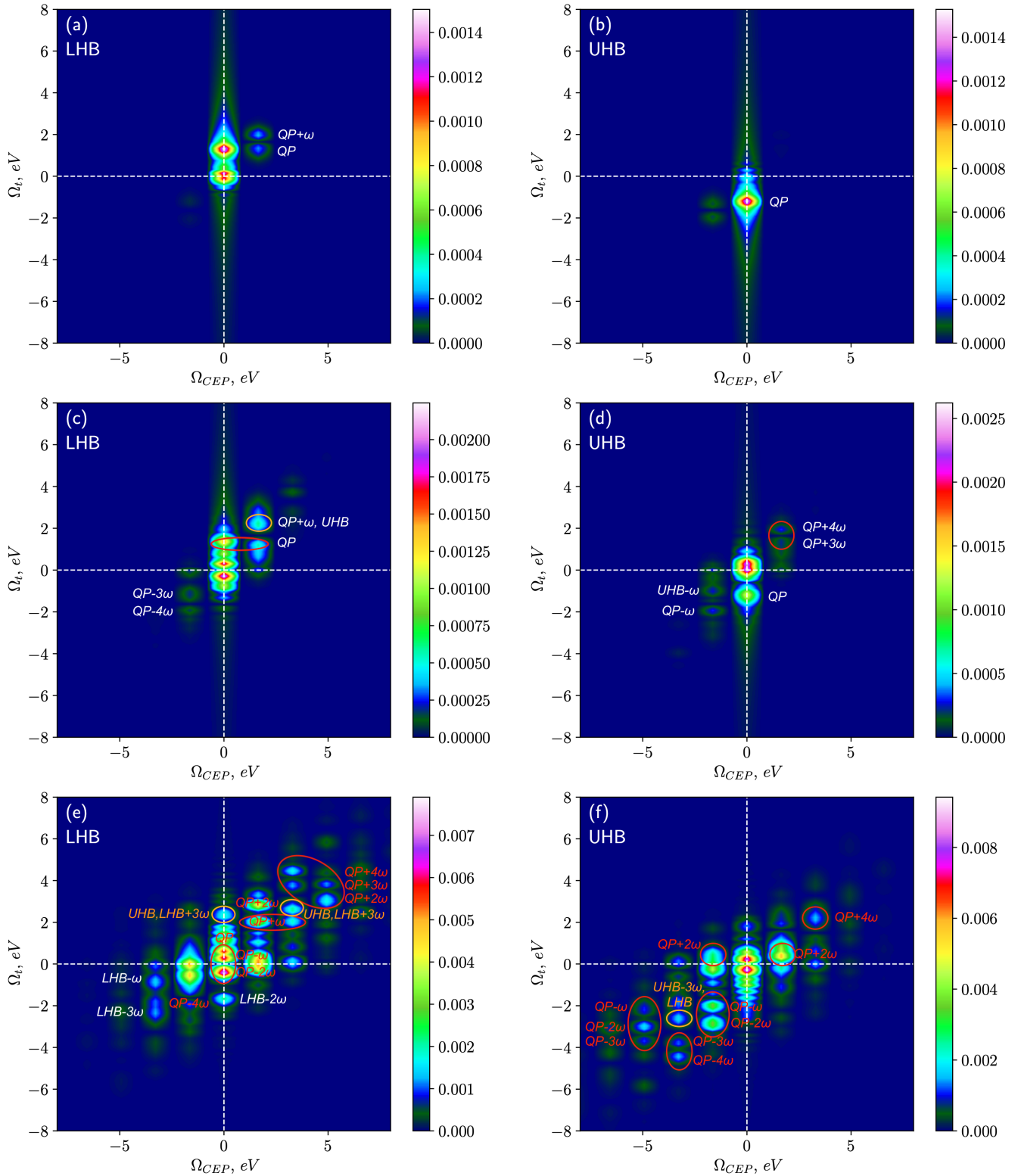


FIG. 3. Multidimensional spectroscopy of correlated electron dynamics. $|G^<(\Omega_\tau, \Omega_t, \Omega_{CEP})|$ vs Ω_t, Ω_{CEP} for $\Omega_\tau = -1.25$ eV (LHB) (a,c,e) and $\Omega_\tau = 1.25$ eV (UHB) (b,d,f) and different field strengths (a,b) $F_0 = 0.1$ V/A, (c,d) $F_0 = 0.5$ V/A, and (e,f) $F_0 = 2$ V/A.

direct non-adiabatic transitions between LHB and UHB (orange circles in Fig 3(e)) become visible, the non-adiabatic transitions are still dominated by the couplings $LHB \leftrightarrow QP$ and $UHB \leftrightarrow QP$.

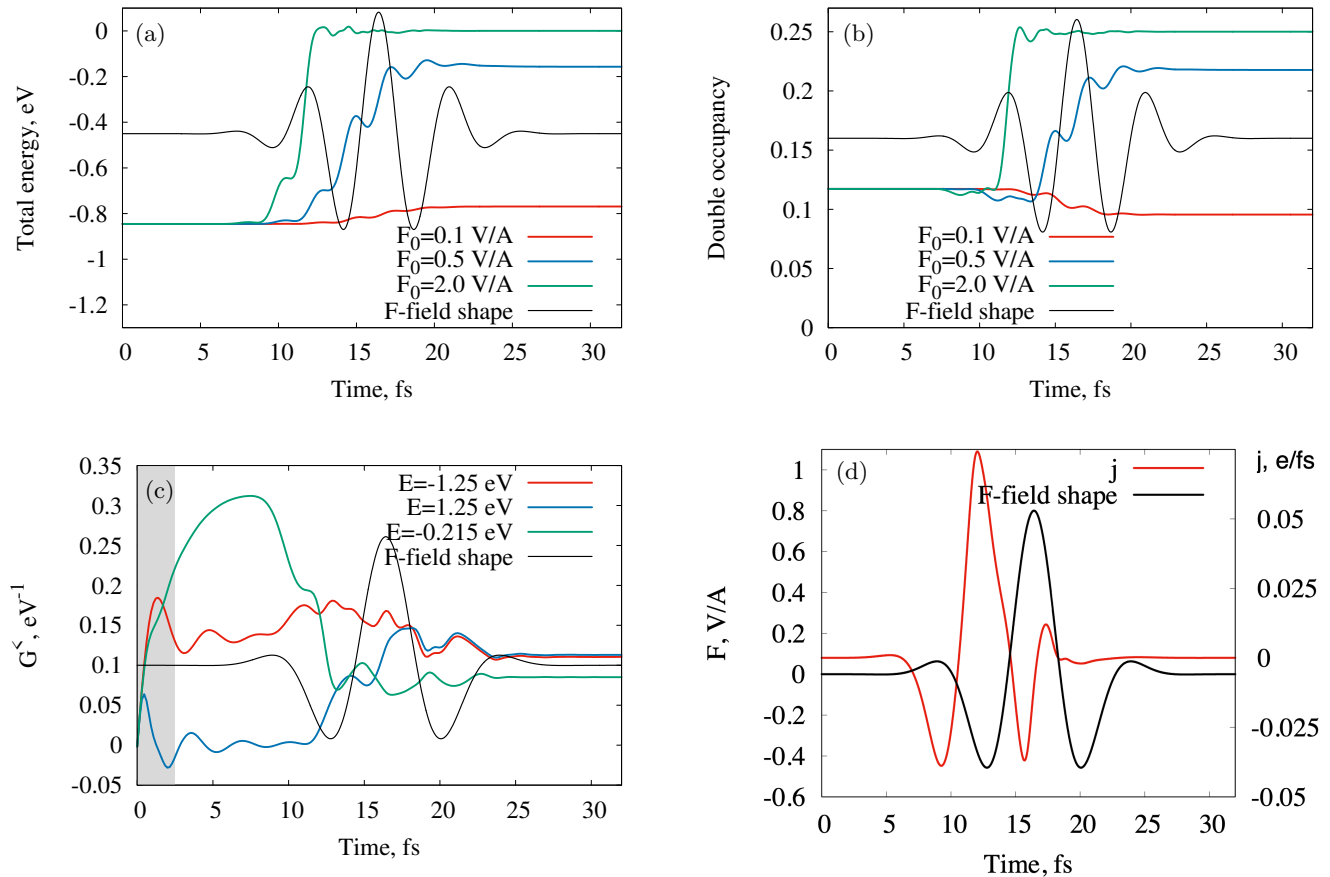


FIG. 4. Temporal dynamics of metal-insulator transition. (a,b) Time-resolved total energy (a) and doublon occupancy (b) for $\omega = 0.827$ eV and various field strengths: $F_0 = 0.1$ V/A (red), 0.5 V/A (blue), 2.0 V/A (green). (c,d) Metal-insulator transition driven by the laser field carried at $\omega = 0.413$ eV. (c) Oscillations of electron density at energies corresponding to *LHB* ($E = -1.25$ eV, red), *UHB* ($E = 1.25$ eV, blue), and *QP* ($E = -0.215$ eV, green) for $F_0 = 0.8$ V/A. (d) Laser pulse (black) and current (red). Onset of locking regime at 18 fs (c) coincides with quenching of current (d).

Indeed, the onset of locking is synchronized with the saturation of energy transfer from the field to the system – the instantaneous total energy of the system during the pulse becomes frozen at its maximum (for a given field strength) value (see Fig 4(a)). For the highest field strength (2 V/A) the maximum energy stabilizes at zero. This fact confirms that population inversion (i.e. achieving higher electron density at *UHB* than at *LHB* energy) is not possible in this regime. Finally, the onset of locking (see Fig 4(c)) is accompanied by the suppression of the current (see Fig 4(d)), which is practically fully quenched at ~ 18 fs (see Fig 4(c,e)), when the insulating state is established. Note that the results presented in Figs 4(c,d) correspond to lower laser field frequency $\omega = 0.413$ eV, demonstrating that our results are not sensitive to the frequency of the intense non-resonant laser field.

Overall, the onset of locking regime is associated with very broad distribution of overlapping laser-dressed states (see Fig 3(e,f)), effectively forming a single band available for electron dynamics. Synchronized cycling of charge flow along the two "circuits" – *LHB* \rightarrow *QP* \rightarrow *LHB* and *UHB* \rightarrow *QP* \rightarrow *UHB* – appear to dominate the dynamical laser-dressed many-body state just before it freezes into the final state after the end of the laser pulse.

In correlated systems, large increase in electron temperature can transform a metal into a bad metallic or insulating-like state. However, in our case, the opening of the gap and the peculiar dynamics observed already within a small fraction of the laser cycle is clearly not thermal. In contrast to phonon-driven transitions [59], our mechanism is purely electronic.

Our findings demonstrate the possibility of manipulating phases of correlated systems with strong non-resonant fields on the sub-cycle time-scale, in a manner that is robust against the frequency of the driving field. While in atoms or molecules such frequency-independent, non-resonant light-induced modifications of the electron density do not persist once the light is turned off, in a strongly correlated solid light-induced changes can lead to persistent modifications surviving after the end of the pulse. The laser pulse can thus transfer the system into a correlated

state inaccessible under equilibrium conditions. In particular for systems close to the Mott transition or with multiple orbital degrees of freedom, this controlled sub-cycle dynamics can offer new mechanisms to control the many body phases, beyond the multi-cycle Floquet engineering. The achieved final state is controlled by charge density and currents shaped on the sub-laser-cycle time-scale, and the spectroscopy introduced here can provide key insights in analysing and designing such excitation pathways.

We thank M. Altarelli for motivating discussions, U. Bovensiepen and M. Ligges for discussions on pump-probe PES of cuprates, and R. E. F. Silva for providing his code for benchmark. This research was supported in part through the European XFEL and DESY computational resources in the Maxwell infrastructure operated at Deutsches Elektronen-Synchrotron (DESY), Hamburg, Germany. This work was supported by the Cluster of Excellence "Advanced Imaging of Matter" of the Deutsche Forschungsgemeinschaft (DFG) - EXC 2056 - project ID390715994. H.A. acknowledges a support from the ImPACT Program of the Council for Science, Technology and Innovation, Cabinet Office, Government of Japan (Grant No. 2015-PM12-05-01) from JST, JSPS KAKENHI Grant No.17H06138, and CREST "Topology" project from JST. M.I. and O.S. acknowledge support of the H2020 European Research Council Optologic grant (899794). The work of A.I.L. and M.I.K. is supported by European Research Council via Synergy Grant 854843 - FASTCORR. M.E. acknowledges funding from the ERC via starting grant No. 716648.

-
- [1] K Kuroda, T Tomita, M-T Suzuki, C Bareille, AA Nugroho, Pallab Goswami, M Ochi, M Ikhlas, M Nakayama, S Akebi, et al. Evidence for magnetic weyl fermions in a correlated metal. *Nature materials*, 16(11):1090–1095, 2017.
 - [2] Jia-Xin Yin, Songtian S Zhang, Hang Li, Kun Jiang, Guoqing Chang, Bingjing Zhang, Biao Lian, Cheng Xiang, Ilya Belopolski, Hao Zheng, et al. Giant and anisotropic many-body spin-orbit tunability in a strongly correlated kagome magnet. *Nature*, 562(7725):91–95, 2018.
 - [3] Barry Bradlyn, Jennifer Cano, Zhijun Wang, M. G. Vergniory, C. Felser, R. J. Cava, and B. Andrei Bernevig. Beyond dirac and weyl fermions: Unconventional quasiparticles in conventional crystals. *Science*, 353(6299):aaf5037, 2016.
 - [4] Gabriel E Topp, Nicolas Tancogne-Dejean, Alexander F Kemper, Angel Rubio, and Michael A Sentef. All-optical nonequilibrium pathway to stabilising magnetic weyl semimetals in pyrochlore iridates. *Nature communications*, 9(1):1–9, 2018.
 - [5] Ferenc Krausz and Misha Ivanov. Attosecond physics. *Reviews of modern physics*, 81(1):163, 2009.
 - [6] Eleftherios Goulielmakis, Vladislav S Yakovlev, Adrian L Cavaleri, Matthias Uiberacker, Volodymyr Pervak, A Apolonski, Reinhard Kienberger, Ulf Kleineberg, and Ferenc Krausz. Attosecond control and measurement: lightwave electronics. *Science*, 317(5839):769–775, 2007.
 - [7] Manish Garg, Minjie Zhan, Tran Trung Luu, H Lakhotia, Till Klostermann, Alexander Guggenmos, and Eleftherios Goulielmakis. Multi-petahertz electronic metrology. *Nature*, 538(7625):359–363, 2016.
 - [8] H Lakhotia, HY Kim, Minjie Zhan, S Hu, S Meng, and Eleftherios Goulielmakis. Laser picoscopy of valence electrons in solids. *Nature*, 583(7814):55–59, 2020.
 - [9] Takashi Oka and Sota Kitamura. Floquet engineering of quantum materials. *Annual Review of Condensed Matter Physics*, 10(1):387–408, 2019.
 - [10] Takahiro Mikami, Sota Kitamura, Kenji Yasuda, Naoto Tsuji, Takashi Oka, and Hideo Aoki. Brillouin-wigner theory for high-frequency expansion in periodically driven systems: Application to floquet topological insulators. *Phys. Rev. B*, 93:144307, Apr 2016.
 - [11] Reinhard Kienberger, Eleftherios Goulielmakis, Matthias Uiberacker, Andrius Baltuska, Vladislav Yakovlev, Ferdinand Bammer, Armin Scrinzi, Th Westerwalbesloh, Ulf Kleineberg, Ulrich Heinzmann, et al. Atomic transient recorder. *Nature*, 427(6977):817–821, 2004.
 - [12] Giuseppe Sansone, Enrico Benedetti, Francesca Calegari, Caterina Vozzi, Lorenzo Avaldi, Roberto Flammini, Luca Poletto, P Villoresi, C Altucci, R Velotta, et al. Isolated single-cycle attosecond pulses. *Science*, 314(5798):443–446, 2006.
 - [13] Federico Ferrari, Francesca Calegari, Matteo Lucchini, Caterina Vozzi, Salvatore Stagira, Giuseppe Sansone, and Mauro Nisoli. High-energy isolated attosecond pulses generated by above-saturation few-cycle fields. *Nature Photonics*, 4(12):875–879, 2010.
 - [14] J Itatani, F Quéré, Gennady L Yudin, M Yu Ivanov, Ferenc Krausz, and Paul B Corkum. Attosecond streak camera. *Physical review letters*, 88(17):173903, 2002.
 - [15] Adrian L Cavaleri, Norbert Müller, Th Uphues, Vladislav S Yakovlev, Andrius Baltuska, Balint Horvath, B Schmidt, L Blümel, R Holzwarth, Stefan Hendel, et al. Attosecond spectroscopy in condensed matter. *Nature*, 449(7165):1029–1032, 2007.
 - [16] Francesca Calegari, D Ayuso, Andrea Trabattini, Louise Belshaw, Simone De Camillis, S Anumula, F Frassetto, L Poletto, A Palacios, P Declava, et al. Ultrafast electron dynamics in phenylalanine initiated by attosecond pulses. *Science*, 346(6207):336–339, 2014.
 - [17] Mauro Nisoli, Piero Declava, Francesca Calegari, Alicia Palacios, and Fernando Martín. Attosecond electron dynamics in molecules. *Chemical reviews*, 117(16):10760–10825, 2017.
 - [18] L Seiffert, Q Liu, Sergey Zherebtsov, A Trabattini, P Rupp, MC Castrovilli, M Galli, Frederik Süßmann, K Wintersperger, Johannes Stierle, et al. Attosecond chronoscopy of electron scattering in dielectric nanoparticles. *Nature physics*, 13(8):766–770, 2017.

- [19] Renate Pazourek, Stefan Nagele, and Joachim Burgdörfer. Attosecond chronoscopy of photoemission. *Reviews of Modern Physics*, 87(3):765, 2015.
- [20] JM Dahlström, Anne L’Huillier, and A Maquet. Introduction to attosecond delays in photoionization. *Journal of Physics B: Atomic, Molecular and Optical Physics*, 45(18):183001, 2012.
- [21] G Vampa, TJ Hammond, N Thiré, BE Schmidt, F Légaré, CR McDonald, T Brabec, and PB Corkum. Linking high harmonics from gases and solids. *Nature*, 522(7557):462–464, 2015.
- [22] REF Silva, Igor V Blinov, Alexey N Rubtsov, O Smirnova, and M Ivanov. High-harmonic spectroscopy of ultrafast many-body dynamics in strongly correlated systems. *Nature Photonics*, 12(5):266–270, 2018.
- [23] REF Silva, Á Jiménez-Galán, B Amorim, O Smirnova, and M Ivanov. Topological strong-field physics on sub-laser-cycle timescale. *Nature Photonics*, 13(12):849–854, 2019.
- [24] Á Jiménez-Galán, REF Silva, O Smirnova, and M Ivanov. Lightwave control of topological properties in 2d materials for sub-cycle and non-resonant valley manipulation. *Nature Photonics*, 14(12):728–732, 2020.
- [25] Álvaro Jiménez-Galán, Rui EF Silva, Olga Smirnova, and Misha Ivanov. Sub-cycle valleytronics: control of valley polarization using few-cycle linearly polarized pulses. *Optica*, 8(3):277–280, 2021.
- [26] Andrius Baltuška, Th Udem, M Uiberacker, M Hentschel, Eleftherios Goulielmakis, Ch Gohle, Ronald Holzwarth, Vladislav S Yakovlev, A Scrinzi, Th W Hänsch, et al. Attosecond control of electronic processes by intense light fields. *Nature*, 421(6923):611–615, 2003.
- [27] Tibor Wittmann, Balint Horvath, Wolfram Helml, Michael G Schätzel, Xun Gu, Adrian L Cavalieri, GG Paulus, and Reinhard Kienberger. Single-shot carrier-envelope phase measurement of few-cycle laser pulses. *Nature Physics*, 5(5):357–362, 2009.
- [28] Eleftherios Goulielmakis, Martin Schultze, M Hofstetter, Vladislav S Yakovlev, Justin Gagnon, M Uiberacker, Andrew L Aquila, EM Gullikson, David T Attwood, Reinhard Kienberger, et al. Single-cycle nonlinear optics. *Science*, 320(5883):1614–1617, 2008.
- [29] L.S. Cederbaum and J. Zobeley. Ultrafast charge migration by electron correlation. *Chemical Physics Letters*, 307(3):205–210, 1999.
- [30] F. Remacle, R. D. Levine, E. W. Schlag, and R. Weinkauf. Electronic control of site selective reactivity: A model combining charge migration and dissociation. *The Journal of Physical Chemistry A*, 103(49):10149–10158, 1999.
- [31] Siegfried Lünemann, Alexander I. Kuleff, and Lorenz S. Cederbaum. Ultrafast charge migration in 2-phenylethyl-n,n-dimethylamine. *Chemical Physics Letters*, 450(4):232–235, 2008.
- [32] J. Breidbach and L. S. Cederbaum. Migration of holes: Formalism, mechanisms, and illustrative applications. *The Journal of Chemical Physics*, 118(9):3983–3996, 2003.
- [33] F. Remacle and R. D. Levine. An electronic time scale in chemistry. *Proceedings of the National Academy of Sciences*, 103(18):6793–6798, 2006.
- [34] Alexander I Kuleff and Lorenz S Cederbaum. Ultrafast correlation-driven electron dynamics. *Journal of Physics B: Atomic, Molecular and Optical Physics*, 47(12):124002, jun 2014.
- [35] Francesca Calegari, Giuseppe Sansone, Salvatore Stagira, Caterina Vozzi, and Mauro Nisoli. Advances in attosecond science. *Journal of Physics B: Atomic, Molecular and Optical Physics*, 49(6):062001, feb 2016.
- [36] Naoto Tsuji, Takashi Oka, Hideo Aoki, and Philipp Werner. Repulsion-to-attraction transition in correlated electron systems triggered by a monocycle pulse. *Physical Review B*, 85(15):155124, 2012.
- [37] Naoto Tsuji, Takashi Oka, Philipp Werner, and Hideo Aoki. Dynamical band flipping in fermionic lattice systems: An ac-field-driven change of the interaction from repulsive to attractive. *Physical Review Letters*, 106(23):236401, 2011.
- [38] DN Basov, RD Averitt, and D Hsieh. Towards properties on demand in quantum materials. *Nature materials*, 16(11):1077–1088, 2017.
- [39] Martin Schultze, Markus Fieß, Nicholas Karpowicz, Justin Gagnon, Michael Korbman, Michael Hofstetter, S Neppl, Adrian L Cavalieri, Yannis Komninos, Th Mercouris, et al. Delay in photoemission. *science*, 328(5986):1658–1662, 2010.
- [40] Marcus Ossiander, Johann Riemensberger, S Neppl, M Mittermair, Martin Schäffer, A Duensing, MS Wagner, R Heider, M Wurzer, M Gerl, et al. Absolute timing of the photoelectric effect. *Nature*, 561(7723):374–377, 2018.
- [41] Annkatrin Sommer, EM Bothschafter, SA Sato, Clemens Jakubeit, Tobias Latka, Olga Razzkazovskaya, Hanieh Fattahi, Michael Jobst, W Schweinberger, Vage Shirvanyan, et al. Attosecond nonlinear polarization and light-matter energy transfer in solids. *Nature*, 534(7605):86–90, 2016.
- [42] Christoph P Schmid, Leonard Weigl, P Grössing, Vanessa Junk, Cosimo Gorini, Stefan Schlauderer, Suguru Ito, Manuel Meierhofer, Niklas Hofmann, Dmitry Afanasiev, et al. Tunable non-integer high-harmonic generation in a topological insulator. *Nature*, 593(7859):385–390, 2021.
- [43] Markus Ludwig, Garikoitz Aguirregabiria, Felix Ritzkowsky, Tobias Rybka, Dana Codruta Marinica, Javier Aizpurua, Andrei G Borisov, Alfred Leitenstorfer, and Daniele Brida. Sub-femtosecond electron transport in a nanoscale gap. *Nature Physics*, 16(3):341–345, 2020.
- [44] William P Putnam, Richard G Hobbs, Phillip D Keathley, Karl K Berggren, and Franz X Kärtner. Optical-field-controlled photoemission from plasmonic nanoparticles. *nature physics*, 13(4):335–339, 2017.
- [45] Takuya Higuchi, Christian Heide, Konrad Ullmann, Heiko B Weber, and Peter Hommelhoff. Light-field-driven currents in graphene. *Nature*, 550(7675):224–228, 2017.
- [46] David Ayuso, Ofer Neufeld, Andres F Ordonez, Piero Decleva, Gavriel Lerner, Oren Cohen, Misha Ivanov, and Olga Smirnova. Synthetic chiral light for efficient control of chiral light-matter interaction. *Nature Photonics*, 13(12):866–871, 2019.

- [47] Alexander V Joura, JK Freericks, and Alexander I Lichtenstein. Long-lived nonequilibrium states in the hubbard model with an electric field. *Physical Review B*, 91(24):245153, 2015.
- [48] Camille Aron, Gabriel Kotliar, and Cedric Weber. Dimensional crossover driven by an electric field. *Physical review letters*, 108(8):086401, 2012.
- [49] P Schmidt and H Monien. Nonequilibrium dynamical mean-field theory of a strongly correlated system. *arXiv preprint cond-mat/0202046*, 2002.
- [50] Hideo Aoki, Naoto Tsuji, Martin Eckstein, Marcus Kollar, Takashi Oka, and Philipp Werner. Nonequilibrium dynamical mean-field theory and its applications. *Reviews of Modern Physics*, 86(2):779, 2014.
- [51] Antoine Georges, Gabriel Kotliar, Werner Krauth, and Marcelo J Rozenberg. Dynamical mean-field theory of strongly correlated fermion systems and the limit of infinite dimensions. *Reviews of Modern Physics*, 68(1):13, 1996.
- [52] Martin Eckstein, Marcus Kollar, and Philipp Werner. Interaction quench in the hubbard model: Relaxation of the spectral function and the optical conductivity. *Phys. Rev. B*, 81:115131, Mar 2010.
- [53] Michael Schüler, Denis Golež, Yuta Murakami, Nikolaj Bittner, Andreas Herrmann, Hugo U.R. Strand, Philipp Werner, and Martin Eckstein. Nessi: The non-equilibrium systems simulation package. *Computer Physics Communications*, 257:107484, 2020.
- [54] R. S. Markiewicz, S. Sahrakorpi, M. Lindroos, Hsin Lin, and A. Bansil. One-band tight-binding model parametrization of the high- T_c cuprates including the effect of k_z dispersion. *Phys. Rev. B*, 72:054519, Aug 2005.
- [55] J.-Y. P. Delannoy, M. J. P. Gingras, P. C. W. Holdsworth, and A.-M. S. Tremblay. Low-energy theory of the $t - t' - t'' - u$ hubbard model at half-filling: Interaction strengths in cuprate superconductors and an effective spin-only description of La_2CuO_4 . *Phys. Rev. B*, 79:235130, Jun 2009.
- [56] Gabriel Kotliar and Dieter Vollhardt. Strongly correlated materials: Insights from dynamical mean-field theory. *Physics Today*, 57(3):53–59, 2004.
- [57] Francesco Randi, Daniele Fausti, and Martin Eckstein. Bypassing the energy-time uncertainty in time-resolved photoemission. *Physical Review B*, 95(11):115132, 2017.
- [58] Klaus Reimann, Michael Woerner, and Thomas Elsaesser. Two-dimensional terahertz spectroscopy of condensed-phase molecular systems. *The Journal of Chemical Physics*, 154(12):120901, 2021.
- [59] Michael Först, Cristian Manzoni, Stefan Kaiser, Yasuhide Tomioka, Yoshi-nori Tokura, Roberto Merlin, and Andrea Cavalleri. Nonlinear phononics as an ultrafast route to lattice control. *Nature Physics*, 7(11):854–856, 2011.
- [60] Naoto Tsuji, Takashi Oka, and Hideo Aoki. Correlated electron systems periodically driven out of equilibrium: Floquet+dmft formalism. *Physical Review B*, 78(23):235124, 2008.
- [61] JK Freericks, HR Krishnamurthy, and Th Pruschke. Theoretical description of time-resolved photoemission spectroscopy: application to pump-probe experiments. *Physical review letters*, 102(13):136401, 2009.

I. METHODS

A. Simulations

The Hamiltonian is

$$H(t) = \sum_{ij\sigma} T_{ij}(t) c_{i\sigma}^\dagger c_{j\sigma} + U \sum_i (n_{i\uparrow} - \frac{1}{2})(n_{i\downarrow} - \frac{1}{2}), \quad (1)$$

where i, j label the lattice sites, U is the on-site Coulomb interaction, $c_{i\sigma}^\dagger$ ($c_{j\sigma}$) are the fermionic creation (annihilation) operators for site i (j) and spin σ , $n_{i\sigma} = c_{i\sigma}^\dagger c_{i\sigma}$ is the particle number operator. The hopping amplitudes $T_{ij}(t)$ between the sites i and j include the nearest-neighbor (T_1) and the next-neighbor (T_2) terms. The external low-frequency laser field (frequency $\omega < U, W = 8T_1$) is included via the Peierls substitution,

$$T_{ij}(t) = \sum_{ij} T_{ij} \exp\left(-i \int_{\mathbf{R}_j}^{\mathbf{R}_i} d\mathbf{r} \cdot \mathbf{A}(t)\right), \quad (2)$$

where $\mathbf{A}(t)$ is the field vector-potential, $\mathbf{F}(t) = -\partial\mathbf{A}(t)/\partial t$. The one-particle dispersion is

$$\begin{aligned} \varepsilon(k, t) = & 2T_1[\cos(k_x + \mathbf{A}_x(t)) + \cos(k_y + \mathbf{A}_y(t))] \\ & + 4T_2[\cos(k_x + \mathbf{A}_x(t)) \cdot \cos(k_y + \mathbf{A}_y(t))]. \end{aligned} \quad (3)$$

The total energy $E_{\text{tot}}(t) = E_{\text{kin}}(t) + E_{\text{pot}}(t)$ includes potential and kinetic terms,

$$E_{\text{pot}}(t) = U \langle (n_{\uparrow} - \frac{1}{2})(n_{\downarrow} - \frac{1}{2}) \rangle, \quad (4)$$

$$E_{\text{kin}}(t) = -i \sum_{\mathbf{k}} \varepsilon_{\mathbf{k}} G_{\mathbf{k}+\mathbf{A}(t)}^<(t, t), \quad (5)$$

where $\tilde{G}_{\mathbf{k}}^{\leq}(t, t)$ is the gauge-invariant [60] lesser Green function. The momentum distribution function is

$$n(\mathbf{k}, t) = f(\mathbf{k}, t) = -i\tilde{G}_{\mathbf{k}}^{\leq}(t, t) = -iG_{\mathbf{k}+\mathbf{A}(t)}^{\leq}(t, t). \quad (6)$$

The population density is calculated as

$$G^{\leq}(\omega, t) = \frac{1}{\pi} \text{Im} \int ds e^{i\omega s} G^{\leq}(t, t-s). \quad (7)$$

Due to the limitation in time data, the selected Fourier transform produces some blur on the graph of occupied states for the first 5 fs.

The time-resolved photoemission intensity is given by

$$I(\omega, t_p) = -i \int dt dt' S(t) S(t') e^{i\omega(t-t')} G^{\leq}(t + t_p, t' + t_p), \quad (8)$$

where $S(t - t_p)$ is the envelope of the probe pulse centered at t_p [57].

B. Spectroscopic nature of the double-time lesser Green's function

The double-time lesser Green's function provides information about the spectrum of occupied states of the system and is indispensable for visualizing electronic structure and dynamics. Starting from its definition:

$$G_{ij}^{\leq}(t, t - \tau) = i \langle c_i^{\dagger}(t - \tau) c_j(t) \rangle \quad (9)$$

we review the emergence of laser-dressed states in its structure as well as their visualization via G_{ij}^{\leq} , available in any calculation of electronic structure or dynamics in a solid. Rewriting Eq. (9) explicitly by introducing the eigenstates $|m\rangle$ of N -electron system

$$G_{ij}^{\leq}(t, t - \tau) = i \sum_m \langle m | \mathcal{T} e^{i \int_0^{t-\tau} H(t') dt'} c_i^{\dagger} \mathcal{T} e^{-i \int_0^t H(t') dt'} \mathcal{T} e^{i \int_0^t H(t') dt'} c_j \mathcal{T} e^{-i \int_0^t H(t') dt'} | m \rangle, \quad (10)$$

applying propagators to eigenstates $|\Psi_m(t)\rangle = e^{-i \int_0^t H(t') dt'} |m\rangle$ and inserting the resolution of identity $I = \sum_n |n\rangle \langle n|$ on the eigenstates of $(N-1)$ -electron system we obtain:

$$G_{ij}^{\leq}(t, t - \tau) = i \sum_{m,n} \langle \Psi_m(t - \tau) | c_i^{\dagger} \mathcal{T} e^{-i \int_0^{t-\tau} H(t') dt'} | n \rangle \langle n | \mathcal{T} e^{i \int_0^t H(t') dt'} c_j | \Psi_m(t) \rangle. \quad (11)$$

After time propagation Eq. (11) reduces to the following equation:

$$G_{ij}^{\leq}(t, t - \tau) = i \sum_{m,n} \langle \Psi_m(t - \tau) | c_i^{\dagger} | \Psi_n(t - \tau) \rangle \langle \Psi_n(t) | c_j | \Psi_m(t) \rangle. \quad (12)$$

Consider the typical Floquet regime corresponding to CW pulse. The laser-dressed states can be written as:

$$\Psi_m(t) = e^{-i\mathcal{E}_m t} f_m(t), \quad \Psi_n(t) = e^{-i\mathcal{E}_n t} f_n(t), \quad (13)$$

where \mathcal{E}_m (\mathcal{E}_n) is the quasienergy of a Floquet state m (n) and $f_m(t)$ ($f_n(t)$) is a periodic function of time. Introducing auxiliary functions $\Phi_{nm}(t)$, $\Phi_{mn}^{(+)}(t - \tau)$

$$\Phi_{nm}(t) \equiv \langle \Psi_n(t) | c_j | \Psi_m(t) \rangle = e^{i(\mathcal{E}_n - \mathcal{E}_m)t} f_{nm}(t), \quad (14)$$

$$\Phi_{mn}^{(+)}(t - \tau) \equiv \langle \Psi_m(t - \tau) | c_i^{\dagger} | \Psi_n(t - \tau) \rangle = e^{-i\mathcal{E}_n(t-\tau) + i\mathcal{E}_m(t-\tau)} f_{mn}(t - \tau), \quad (15)$$

we can rewrite the expression for Green's function

$$G_{ij}^{\leq}(t, t - \tau) = i \sum_{m,n} \Phi_{mn}^{(+)}(t - \tau) \Phi_{nm}(t) = \sum_{m,n} f_{mn}(t - \tau) f_{nm}(t) e^{-i(\mathcal{E}_m - \mathcal{E}_n)\tau} \quad (16)$$

Since the functions $f_{mn}(t), f_{nm}(t - \tau)$ are periodic, we can expand them in Fourier series:

$$f_{nm}(t) = \sum_k a_k^{nm} e^{i\omega k t}, \quad (17)$$

$$f_{mn}(t - \tau) = \sum_{k'} a_{k'}^{mn} e^{-i\omega k' (t - \tau)}. \quad (18)$$

Thus,

$$G_{ij}^<(t, t - \tau) = i \sum_{m,n} \sum_{k',l} a_{k'}^{mn} a_{k'+l}^{nm} e^{-il\omega t} e^{-i(\mathcal{E}_m - \mathcal{E}_n + k'\omega)\tau} \quad (19)$$

and the Fourier transform wrt τ yields $\Omega_\tau = \mathcal{E}_m - \mathcal{E}_n + k'\omega$, where $\mathcal{E}_m - \mathcal{E}_n$ represent spectral energies on the vertical axis of Fig 1(a,c,e). If we fix $\Omega_\tau = -1.25$ eV (*LHB*), then $k' = 0$. Fourier transforming Eq. 19 wrt t we obtain $\Omega_t = l\omega$ and a_l^{nm} are the amplitudes of the Floquet ladder starting from zero energy, i.e. the Floquet ladder corresponding to *LHB* for $\Omega_\tau = -1.25$ eV. Thus, in the standard Floquet picture, fixing $\Omega_\tau = E$ (as it is done in Fig3) leads to observation of standard Floquet ladder from the state E .

The situation changes dramatically in the presence of non-adiabatic transitions between the Floquet states. Suppose such non-adiabatic transition couples the N-electron Floquet state m to another N-electron Floquet state m' . Then

$$\Phi_{nm}(t) = \lambda_{mm}(t) e^{i(\mathcal{E}_n - \mathcal{E}_m)t} f_{nm}(t) + \lambda_{m'm}(t) e^{i(\mathcal{E}_n - \mathcal{E}_{m'})t} f_{nm'}(t), \quad (20)$$

and

$$\Phi_{mn}^{(+)}(t - \tau) = \lambda_{mm}(t - \tau) e^{-i(\mathcal{E}_n - \mathcal{E}_m)(t - \tau)} f_{mn}(t - \tau) + \lambda_{m'm'}(t - \tau) e^{-i(\mathcal{E}_n - \mathcal{E}_{m'})(t - \tau)} f_{m'n}(t - \tau), \quad (21)$$

where the coefficients $\lambda_{mm'}(t)$ represent the amplitudes of non-adiabatic transitions between the quasienergies \mathcal{E}_m and $\mathcal{E}_{m'}$. In this case, the product $\Phi_{mn}(t - \tau)\Phi_{nm}(t)$, contributing to $G_{ij}^<(t, t - \tau)$ in Eq.(16), acquires three additional terms (Eqs. (23-25)):

$$\Phi_{mn}(t - \tau)\Phi_{nm}(t) = \lambda_{mm}(t)\lambda_{mm}(t - \tau) f_{nm}(t) f_{mn}(t - \tau) e^{i(\mathcal{E}_n - \mathcal{E}_m)\tau} + \quad (22)$$

$$\lambda_{m'm}(t)\lambda_{mm}(t - \tau) f_{nm'}(t) f_{mn}(t - \tau) e^{i(\mathcal{E}_m - \mathcal{E}_{m'})t} e^{i(\mathcal{E}_n - \mathcal{E}_m)\tau} + \quad (23)$$

$$\lambda_{mm}(t)\lambda_{m'm'}(t - \tau) f_{nm}(t) f_{m'n}(t - \tau) e^{i(\mathcal{E}_{m'} - \mathcal{E}_m)t} e^{i(\mathcal{E}_n - \mathcal{E}_{m'})\tau} + \quad (24)$$

$$\lambda_{m'm}(t)\lambda_{m'm'}(t - \tau) f_{nm'}(t) f_{m'n}(t - \tau) e^{i(\mathcal{E}_n - \mathcal{E}_{m'})\tau}. \quad (25)$$

Non-adiabatic transitions from state with quasienergy \mathcal{E}_m to state with quasienergy $\mathcal{E}_{m'}$ lead to new features in the spectrum both along Ω_τ and Ω_t dimensions. Indeed, while the term Eq.(22) is similar to Eq. (16), the term Eq.(25) adds new frequency to the spectrum along Ω_τ dimension. In addition, terms represented by Eqs. (23,24) oscillate (in time t) at "new" frequencies $\pm(\mathcal{E}_{m'} - \mathcal{E}_m)$, which will appear along Ω_t direction. Thus, we see that non-adiabatic transitions lead to significant restructuring of the spectrum encoded in $G_{ij}^<(t, t - \tau)$ and revealed after Fourier transforms wrt to τ and t .

To reveal the time-scale of non-adiabatic transitions we need to employ the additional dimension, sensitive to sub-laser cycle features of electron dynamics. The carrier-envelope phase (CEP) is a natural choice. Scanning CEP we obtain $G_{ij}^<(t, t - \tau, t_{CEP})$. Fourier transform wrt t_{CEP} allows us to tag each non-adiabatic transition and quantify the role of sub-laser cycle dynamics in restructuring the spectrum of the system and in the formation of the final insulating state.

C. Removing trivial CEP dependence

In a long laser pulse, the dependence of the instantaneous electric field on the CEP amounts to the overall time shift $t' = t + t_{CEP}$. This trivial dependence is of no interest and should be removed when analysing the Green's function $G_{ij}^<(t, t - \tau, t_{CEP})$. To see how this should be done, let us assume for the moment that its CEP dependence amounts only to the overall time shift of the argument $t' = t + t_{CEP}$:

$$\tilde{G}_{ij}^<(t, t - \tau, t_{CEP}) = \tilde{G}_{ij}^<(t', t' - \tau). \quad (26)$$

If this is the case, the Green's function should obey the following equation:

$$\frac{\partial G_{ij}^<}{\partial t}(t, t - \tau, t_{CEP}) = \frac{\partial G_{ij}^<}{\partial t_{CEP}}(t, t - \tau, t_{CEP}). \quad (27)$$

Therefore, differentiating the Green's function $G_{ij}^<(t, t - \tau, t_{CEP})$ with respect to t and t_{CEP} and subtracting the resulting terms we obtain the differential contribution $\Delta G_{ij}^<(t, t - \tau, t_{CEP})$, which no longer contains the trivial dependence:

$$\Delta G_{ij}^<(t, t - \tau, t_{CEP}) = \frac{\partial G_{ij}^<}{\partial t}(t, t - \tau, t_{CEP}) - \frac{\partial G_{ij}^<}{\partial t_{CEP}}(t, t - \tau, t_{CEP}). \quad (28)$$

We use $\Delta G_{ij}^<(t, t - \tau, t_{CEP})$ for building the 2D spectroscopy maps as a function of Ω_t and Ω_{CEP} .

D. Recovering full Green's function from photo-electron measurements.

While time and angular-resolved photoemission (trARPES) experiments are directly related to the Green's function, going back from trARPES to the Green's function is nontrivial. In particular, analyzing the photoemission from a single pulse is restricted by energy-time uncertainty [61]. The multi-pulse spectroscopy does not suffer from this limitation, and allows for full retrieval of the Green function, see e.g [57] and discussion below.

The full information in the Green's function can be retrieved by suitable measurements, e.g., exploiting the dependence of the photoemission signal on the phase delay between interfering parts of the photoemission pulse [57]. With this in mind, we can say that $G^<(t, t - \tau)$ emulates the photoionization signal arising from the interference of two photo-ionization events at t and $t - \tau$, which we will refer to as the $P1$ and $P2$ pulse in the following.

To demonstrate how a time-resolved photo-emission experiment may in principle resolve the full Green's function, we start from the general expression given in Ref. [61],

$$I(\omega, t_p) = \int dt dt' e^{i\omega(t-t')} (-i) G^<(t, t') s(t) s(t')^*, \quad (29)$$

where orbital and momentum indices are omitted for simplicity, ω is the frequency of a probe pulse, and $s(t)$ its envelope. It is easy to see that a single Gaussian probe pulse of width δt implies a measurement of $G^<(\omega, t)$ with an uncertainty-limited filter in time and frequency. However, with suitable pulses, Eq. (29) shows that in principle the full time dependence can be retrieved from experiment. For example, to measure $G^<(t, t')$ in a given time window, we choose an orthonormal basis $\phi_n(t)$ for time-dependent functions in that interval, and expand $-iG^<(t, t') = \sum_{n, n'} \phi_n^*(t) g_{n, n'} \phi_{n'}(t')$. The matrix $g_{n, n'}$ is hermitian and positive definite. A probe pulse $S(t) = \phi_n(t)$ then measures the diagonal components, $I^< = g_{n, n}$. A probe pulse $S(t) = \phi_n(t) + e^{i\varphi} \phi_m(t)$ gives $I^< = g_{n, n} + g_{m, m} + e^{-i\varphi} g_{n, m} + e^{i\varphi} g_{m, n}$, so that off-diagonal components $g_{n, m}$ can be obtained by scanning the phase difference φ .

II. SUPPLEMENTARY INFORMATION

A. Cycle-averaged Floquet picture

Here we show that the metal-insulator transition we find in our simulations can not be understood in terms of the simple cycle-averaged picture, which underlies the standard mechanism of Floquet engineering. It becomes clear after the analysis of results of laser-driven dynamics at the lowest field strength $F_0 = 0.1$ V/Å, shown in Fig.5. Comparing the prediction based on the cycle averaged picture shown in Fig.5(a), which uses renormalized hoppings, with the full simulation shown in Fig.5(b), we see that panel (a) does not describe our observations. Specifically, the red curve in Fig.5(a) presents equilibrium density of occupied states calculated with renormalized hoppings $T_{ij}^{eff} = T_{ij} J_0(\mathbf{A}\mathbf{R}_{ij})$ and the same U (i.e. $U = 2.5$ eV). It is essentially identical to the electron density prior to the pulse, because for $F_0 = 0.1$ V/Å the Bessel function $J_0 \simeq 1$, meaning that the hoppings are hardly modified. In Fig.5(b) (identical to Fig.1a) we see that at about 17.5 fs the peak of the density is shifted towards the energy around -1.25 eV. Remarkably it stays there after the field is off. The cycle averaged picture (panel (a), red curve) suggests that the peak of the density should be around zero energy at all times. The stark contrast between the density in Fig.5a and the density on in Fig.5b after 17.5 fs means that the sub-cycle modification of the electron density is crucial for establishing the state of the system observed after 17.5 fs and after the pulse is off.

B. Temporal dynamics in the locking regime

We have established three different regimes of electron dynamics, described in Fig. 1 (b,d,f). Here we focus on the most interesting regime prominent at $F_0 = 2$ V/Å, which corresponds to pronounced locked oscillations of electron

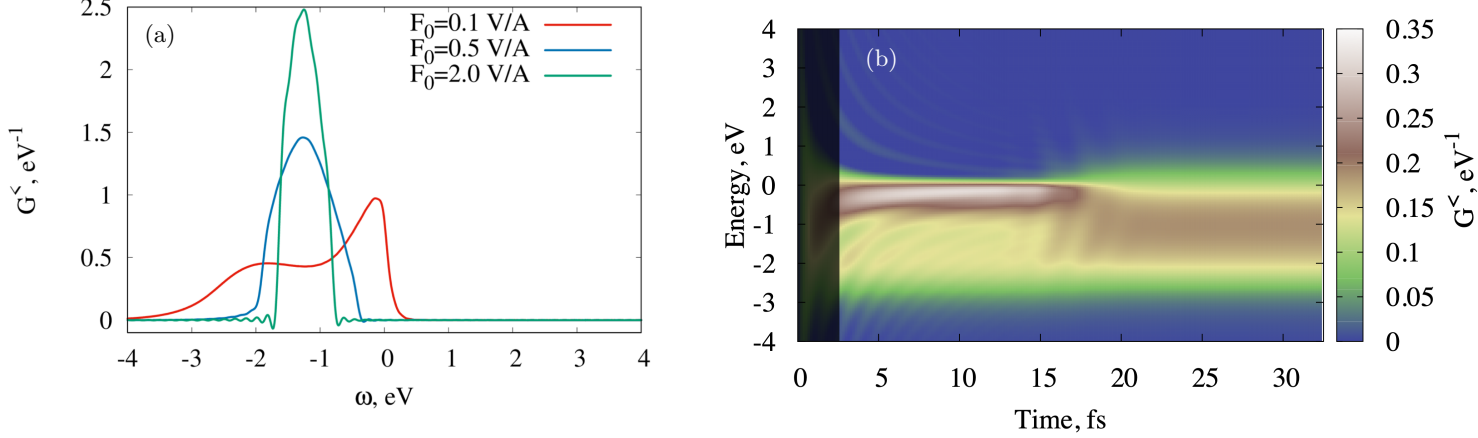


FIG. 5. (a) Equilibrium density of occupied states calculated with renormalized hoppings $T_{ij}^{eff} = T_{ij}J_0(\mathbf{A}\mathbf{R}_{ij})$ and the same U (i.e. $U = 2.5$ eV). Renormalization yields: $T_{ij}^{eff} = T_{ij}J_0(0.32) = 0.9745T_{ij}$ (for $F_0 = 0.1$ V/A); $T_{ij}^{eff} = T_{ij}J_0(1.6) = 0.45T_{ij}$ (for $F_0 = 0.5$ V/A); $T_{ij}^{eff} = T_{ij}J_0(6.4) = 0.24T_{ij}$ (for $F_0 = 2$ V/A.) (b) Fig.1a of the paper reflecting temporal evolution of density of states for $F_0 = 0.1$ V/A.

densities at LHB (red) and UHB (blue) energies: after 13 fs the populations at these energies are nearly equal, locked in phase, and oscillate out of phase with the electron density at the QP energy (green). Here we provide additional information to show that these oscillations are well synchronized with the instantaneous electric field.

Fig. 6 (a) specifies the time instants at which the instantaneous field is $F(t) = 0$. It shows that the populations at LHB (red) and UHB (blue) reach maxima just before the instantaneous zero of the field. The instantaneous rate of population decay (time derivative of red (LHB) and blue (UHB) curves) appears to be maximized at $F(t) = 0$. The population at the QP (green) reaches minima at the zeroes of the field.

Fig.6 (b) specifies time instants at which the instantaneous field reaches its maximal value $|F(t)| = F_0$. It shows that the populations in LHB (red) and UHB (blue) reach minima just before the maximum of the field, when the electron density at the energy of QP maximises.

Thus, the charge density oscillates between QP and LHB, UHB and these oscillations are synchronized with the instantaneous field. Figs. 5 and 6 emphasize the importance of the sub-laser cycle dynamics and motivate the development of the sub-cycle multidimensional spectroscopy described in the main text. This spectroscopy allows one to zoom into the sub-cycle electron dynamics and identify dominant pathways of charge flow responsible for the metal-insulator transition in our system.

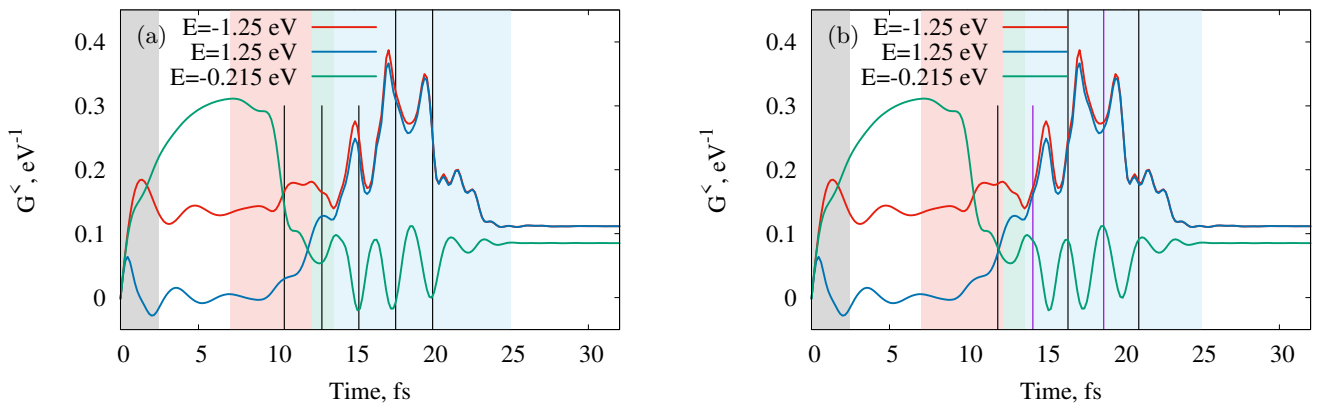


FIG. 6. Temporal oscillations of electron density at the key energies of the system for $F_0 = 2$ V/A, shown vs oscillations of the laser electric field. (a) The vertical lines mark time instants, at which the instantaneous field is equal to zero, $F(t) = 0$. (b) Vertical lines mark time instants, at which the instantaneous field is maximal, $|F(t)| = F_0$.

C. Benchmark simulations

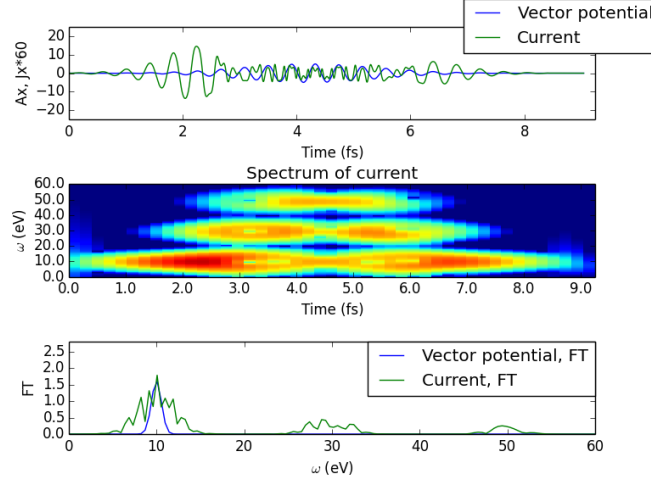


FIG. 7. High harmonic generation on square lattice for gaussian pulse with central frequency $\omega = 10$ eV, $FWHM = 3$ fs, and $A_0 = 5$, polarization along $[10]$ direction. Upper panel: vector potential (blue) and current (green); middle panel: Gabor transform of the current; Lower panel: spectra of incoming pulse (blue) and current (green).

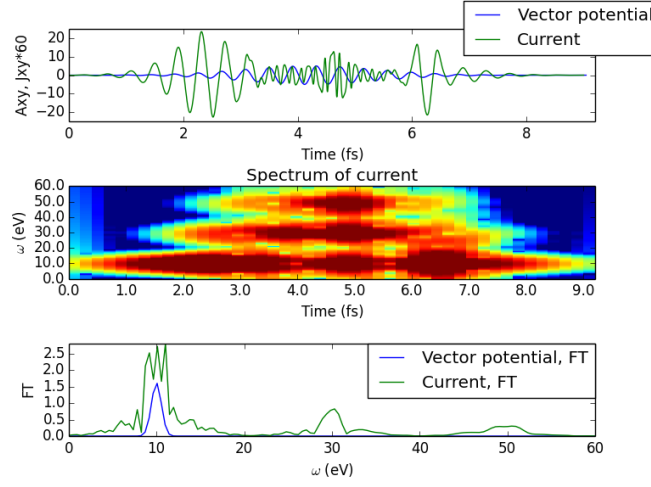


FIG. 8. High harmonic generation on 12-sites chain for Gaussian pulse with central frequency $\omega = 10$ eV, $FWHM = 3$ fs, and $A_0 = 5$, polarization along the chain. Upper panel: vector potential (blue) and current (green); middle panel: Gabor transform of the current; Lower panel: spectra of incoming pulse (blue) and current (green).

We have performed a benchmark of our IPT-DMFT on square lattice to the code described in Ref. 22, performing exact diagonalization for the finite 12-site one-dimensional chain. We set the hoppings $T = 1$ eV, on-site Coulomb repulsion $U = 6$ eV, pulse vector potential amplitude $A_0 = 5$, pulse FWHM is 3fs, pulse central frequency $\omega = 10$ eV. In order to compare our two-dimensional lattice model to one-dimensional chain, we choose linear pulse polarization along $[10]$ direction and relatively large field amplitude.

Although the physics is different between 1D and 2D systems due to the existence of closed loops and additional scattering channels in two dimensions, the resulting HHG spectra look qualitatively similar (see Figs. 7 and 8).